GEOCHEMISTRY

Hydrothermal-derived black carbon as a source of recalcitrant dissolved organic carbon in the ocean

Youhei Yamashita[1,2]*, Yutaro Mori[2], Hiroshi Ogawa[3]

Deep-sea hydrothermal vents are a possible source of thermogenic dissolved black carbon (DBC), which is a component of recalcitrant dissolved organic carbon, but little is known about the distribution of hydrothermal DBC in the deep ocean. Here, we show basin-scale distributions of DBC along two transects in the eastern Pacific Ocean, which are located outside the jet-like hydrothermal plumes from the East Pacific Rise. The DBC concentration in the deep waters did not show a strong linear relationship with apparent oxygen utilization (AOU), as previously observed in the central and western Pacific Ocean. Deviations in DBC concentration from the DBC-AOU relationship observed in the central and western Pacific Ocean were quantified. The deviation was linearly correlated with excess ^{3}He, a tracer for hydrothermal input, indicating that a fraction of the DBC in the deep ocean is transported long distances from hydrothermal systems.

INTRODUCTION

Dissolved organic carbon (DOC) in the ocean represents one of the largest reduced carbon pools on Earth's surface (*1*). The majority is present in the deep ocean, with an average radiocarbon ($\Delta^{14}C$) age of 4000 to 6000 years (*2*, *3*). The stable carbon isotopic signature ($\delta^{13}C$) and lignin phenol content of oceanic DOC imply that its primary source is marine organisms (*3*, *4*). However, our knowledge of the actual origins/production mechanisms and fate of aged (^{14}C-depleted) DOC is still limited (*5*). This information is crucial for understanding the functions of the oceanic DOC pool for carbon sequestration in the global carbon cycle.

Seawater circulation through hydrothermal systems plays a unique role in shaping the DOC concentration and composition in the deep ocean, but its role in the oceanic DOC cycle has not been well elucidated. The ridge-axis hot vents and ridge-flank warm basement outcrops of mid-ocean ridge hydrothermal systems have been considered to act as net sinks for DOC (*6*–*9*), while ridge-axis diffuse flows are suggested to be a net source of DOC (*6*). On the other hand, researchers have suggested that hot hydrothermal vents are sources of thermogenic aromatic DOC in the deep ocean (*10*), and ridge-flank hydrothermal systems have also been shown to supply aromatic DOC (*9*) as well as ^{14}C-depleted DOC produced by chemosynthetic microbes (*11*). Recently, hydrothermal vents have been identified as sources of ^{14}C-depleted DOC, which is transported over long distances in the deep oceans (*12*) based on the observed relationship between the $\Delta^{14}C$ of DOC and excess ^{3}He (nonatmospheric ^{3}He) in the deep ocean (*13*). However, the flux, reactivity, isotopic signature, and chemical structure of ^{14}C-depleted DOC that emanates from hydrothermal vents and is transported long distances have not been identified yet (*12*).

The occurrence of thermogenic DOC in the open ocean has been reported, with suggestions that hydrothermal vents are a major source (*14*). Dissolved black carbon (DBC) is a mixture of condensed aromatic compounds and is determined at the molecular level as it is readily oxidized by concentrated nitric acid to a variety of simple benzenepolycarboxylic acids (BPCAs; mono- through hexa-substituted benzene), which can be easily determined by chromatography (*15*). DBC is characterized as biologically recalcitrant DOC (RDOC) (*16*, *17*) that has been reported to exist throughout the open ocean (*16*, *18*–*23*). Because seawater RDOC, including DBC, has been reported to be removed with hydrothermal circulation (*7*, *24*), researchers have suggested that the DBC present in the ocean is produced through land-based biomass burning and fossil fuel combustion and is transported to the ocean by rivers and atmospheric deposition (*25*, *26*). However, on the basis of evidence of a large mismatch in the $\delta^{13}C$ values between riverine DBC and oceanic DBC, it has recently been indicated that the DBC present in the open ocean does not predominantly originate from rivers (*19*). ^{14}C measurements of oceanic DBC have clarified the ^{14}C-depleted signature of oceanic DBC (~23,000 ± 3000 years) (*27*). In addition, submicrometer-sized graphite particles were found to be derived from high- and low-temperature hydrothermal vents at the East Pacific Rise (EPR) (*28*). These results imply the need to reassess hydrothermal systems as a source of DBC from a basin-scale distribution.

To evaluate whether hydrothermal vents are the sources of DBC in the deep ocean, we determined the basin-scale distribution of DBC in the subtropical North Pacific Ocean and eastern South Pacific Ocean (Fig. 1). Relationships of DBC concentration and composition with ^{3}He, a conservative tracer of hydrothermal input (*29*–*31*), and apparent oxygen utilization (AOU) demonstrate that a fraction of DBC likely originates from hydrothermal systems.

RESULTS AND DISCUSSION

Distribution of DBC in the subtropical North Pacific Ocean and eastern South Pacific Ocean

The DBC concentrations were generally highest in the surface waters (defined as <26.6 σ_θ; approximately <200 m, except for the three southernmost sites) at each site and decreased with depth (Fig. 2). In the surface waters, the (B5CA + B6CA)/total BPCAs, which is an index for the degree of condensation (*15*, *16*), was generally lowest at each site (Fig. 2), implying that the DBC in the

[1]Faculty of Environmental and Earth Science, Hokkaido University, Sapporo, Japan. [2]Graduate School of Environmental Science, Hokkaido University, Sapporo, Japan. [3]Atmosphere and Ocean Research Institute, The University of Tokyo, Kashiwa, Japan.
*Corresponding author. Email: yamashiy@ees.hokudai.ac.jp

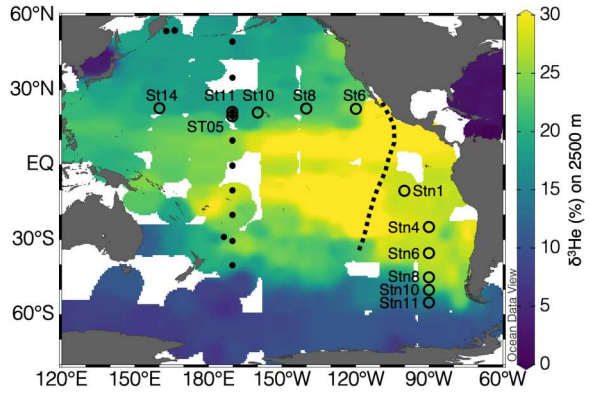

Fig. 1. Spatial distribution of δ^3He values at a depth of approximately 2500 m and the sampling sites. The δ^3He data were derived from Jenkins *et al.* (*30*). The open circles are sampling sites with site numbers in the present study along a zonal transect in the subtropical North Pacific Ocean and a meridional transect in the eastern South Pacific Ocean. The closed circles are sampling sites from Yamashita *et al.* (*16*), which determined the linear relationship between the DBC concentration and AOU in the central and western Pacific Ocean. The black dashed line shows the position of the EPR axis (*37*). Two major helium jets extend westward from the EPR axis at 10°N and at 15°S (*37*).

surface waters could be characterized as less condensed DBC relative to that in the intermediate (defined as 26.6 to 27.5 σ_θ; approximately 200 to 1500 m, depending on the oceanic region) and deep (defined as >27.5 σ_θ; approximately >1500 m) waters. The low degree of condensation in the surface water was likely due to the photodegradation of DBC (*32*, *33*) and/or DBC derived from deposited soot (*34*). The DBC concentration in the surface waters gradually increased from west to east in the subtropical North Pacific Ocean and increased from south to north in the eastern South Pacific Ocean. These spatial gradients for the DBC concentration in the surface waters were similar to those of the annual mean distribution of the surface mass concentration of black carbon (BC) in the atmosphere (*35*), suggesting that deposition of soot from the atmosphere was likely to be the primary source of DBC in the surface waters.

The DBC concentrations in the intermediate and deep waters also showed zonal and meridional gradients in the subtropical North Pacific Ocean and eastern South Pacific Ocean, respectively (Fig. 2). Although a decrease in DBC concentration in the deep waters with an increase in AOU along the deep-ocean meridional circulation routes has recently been observed in the central and western Pacific Ocean (*16*), the DBC concentration in the deep waters did not change with AOU in the present study regions (Fig. 2). The δ^3He values in the deep waters were highest at the easternmost site and the northernmost site in the subtropical North Pacific Ocean and the eastern South Pacific Ocean, respectively (Fig. 2). The high DBC concentrations in the deep waters tended to be coupled with high values of δ^3He (Fig. 2). The spatial distributions of (B5CA + B6CA)/total BPCAs in the deep waters also seemed to be weakly related to those of δ^3He.

Hydrothermal systems as a source of DBC for the deep ocean

A significant negative linear relationship was observed between the DBC concentration and AOU in the deep waters of the central and western Pacific Ocean, and this was suggested to be a result of the removal of DBC from the water column (*16*). To better illustrate differences in the relationship among oceanic regions, relationships between DBC concentration and AOU in the deep waters in the subtropical North Pacific Ocean and eastern South Pacific Ocean were compared with those observed in the central and western Pacific Ocean (Fig. 3) (*16*). The DBC concentrations were not linearly correlated with AOU in each region of the present study. The DBC concentrations in the eastern part of the subtropical North Pacific Ocean and the northern part of the eastern South Pacific Ocean were higher than that predicted by a linear DBC-AOU relationship, suggesting that point sources of DBC are present in the deep oceans. The point sources are relatively close to the EPR axis (Figs. 1 and 2). The core of the mid-depth ^{3}He plume has been observed to spread >4000 km westward from the EPR axis at 15°S, but the plume extends only a short distance (<350 km) eastward of the EPR axis at 15°S (*36*–*38*). The jet-like ^{3}He plume structure has also been observed to extend from the EPR axis to the west at 10°N (*37*). The study sites in the subtropical North Pacific Ocean and in the eastern South Pacific Ocean were located far northwest of and east of the EPR axis, respectively. Thus, the study sites were not affected by the jet-like structure of the ^{3}He plume (Fig. 1). However, ^{3}He was also reported to spread symmetrically 1000 km east to west from the EPR axis at 25°S due to a northward flow along the EPR axis at 25°S and due to the presence of stagnant deep water across the EPR at 25°S (*39*). Therefore, the relatively high and variable δ^3He values obtained at the sites in the present study relative to those in the central and western Pacific Ocean (Fig. 1) (*37*) indicate that the background levels of hydrothermal input were high and variable at the sites due to influences from hydrothermal fluids at the EPR and/or from other hydrothermal vents.

The DBC concentrations in the deep waters at sites that were characterized by relatively high values of δ^3He tended to be higher than those at other sites (Fig. 2), suggesting that the DBC is likely derived from hydrothermal systems. However, the hydrothermal signals for DBC in the transects (Fig. 2) were most likely obscured because of other processes that control DBC in the deep oceans, namely, transport of surface DBC through deep water formations and subsequent removal along with deep-ocean meridional circulation, which shapes the negative DBC-AOU relationship observed in the central and western North Pacific Ocean (*16*). Assuming that the negative DBC-AOU relationship observed in the central and western Pacific Ocean is conservative throughout the Pacific Ocean, the observed deviations from the linear relationship can be considered to be attributed to local sources in the eastern Pacific Ocean. We quantified the deviation and defined it as DBC* (see Materials and Methods for details). Linear relationships were observed between DBC* and excess ^{3}He in the subtropical North Pacific Ocean and eastern South Pacific Ocean (Fig. 4). Notably, the linearity of the relationships between DBC* and excess ^{3}He was much better than those between the bulk DBC concentration and excess ^{3}He (R^2 = 0.248, P = 0.070, n = 14 for the subtropical North Pacific Ocean and R^2 = 0.375, P = 0.015, n = 15 for the eastern South Pacific Ocean; fig. S1) because the effect of the transport of surface DBC through deep water formations and its removal was eliminated for DBC*. The linear relationships indicated that hydrothermal vents were the most likely source of DBC* in the deep waters, and this hydrothermal DBC was transported over long distances in the deep ocean. The higher DBC* is, the higher the

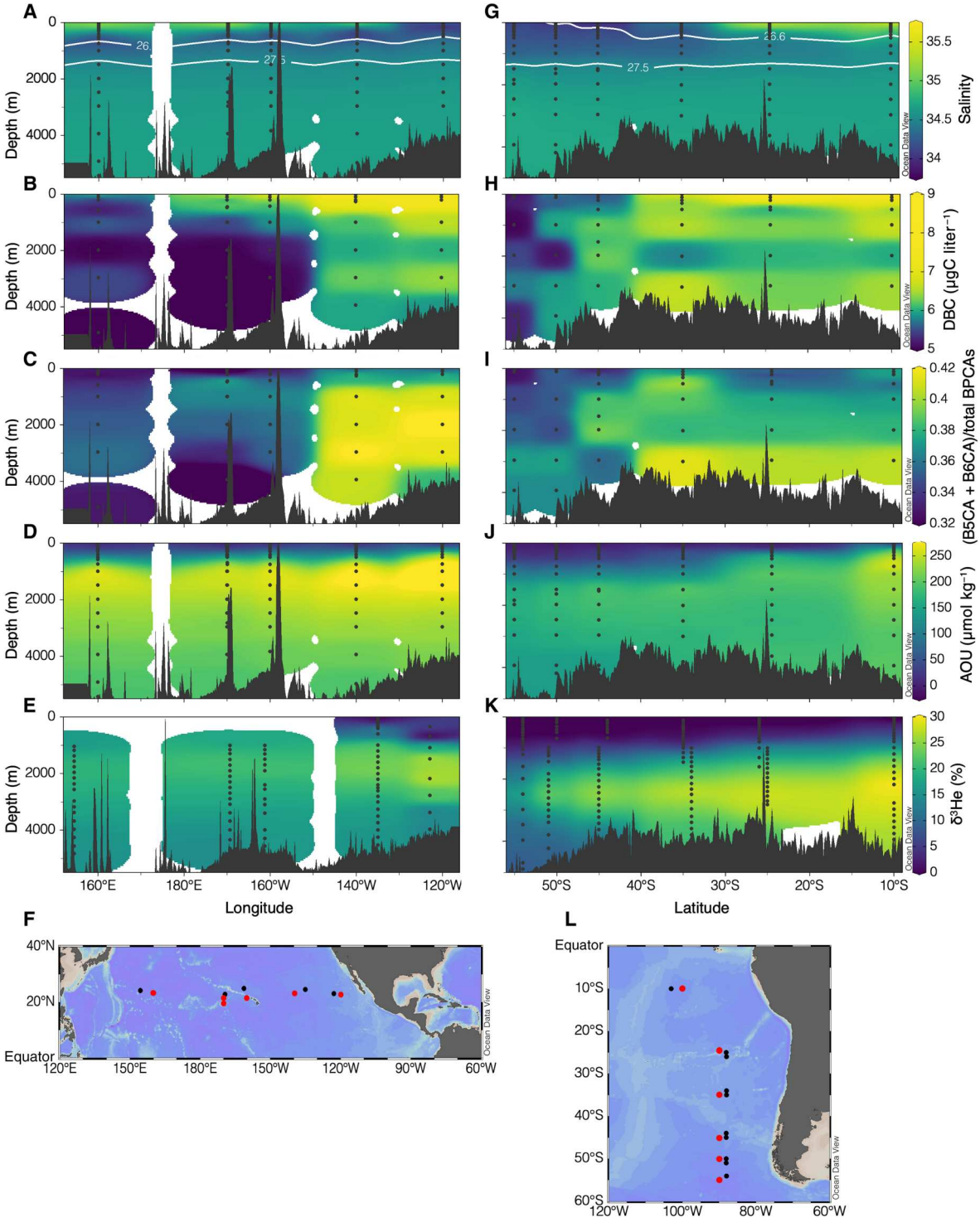

Fig. 2. Basin-scale distributions of DBC. (**A** to **F**) Distributions in the subtropical North Pacific Ocean, salinity with σ_θ (A), DBC concentration (B), (B5CA + B6CA)/total BPCAs (C), AOU (D), δ^3He (E), and sampling sites (F). (**G** to **L**) Distributions in the eastern South Pacific Ocean, salinity with σ_θ (G), DBC concentration (H), (B5CA + B6CA)/total BPCAs (I), AOU (J), δ^3He (K), and sampling sites (L). The color scale of the DBC concentration in (B) and (H) is nonlinear. The δ^3He data in (E) and (K) were derived from Jenkins *et al.* (*30*). The red and black circles in (F) and (L) are sampling sites for salinity, DBC, and AOU in the present study and those for δ^3He from Jenkins *et al.* (*30*), respectively.

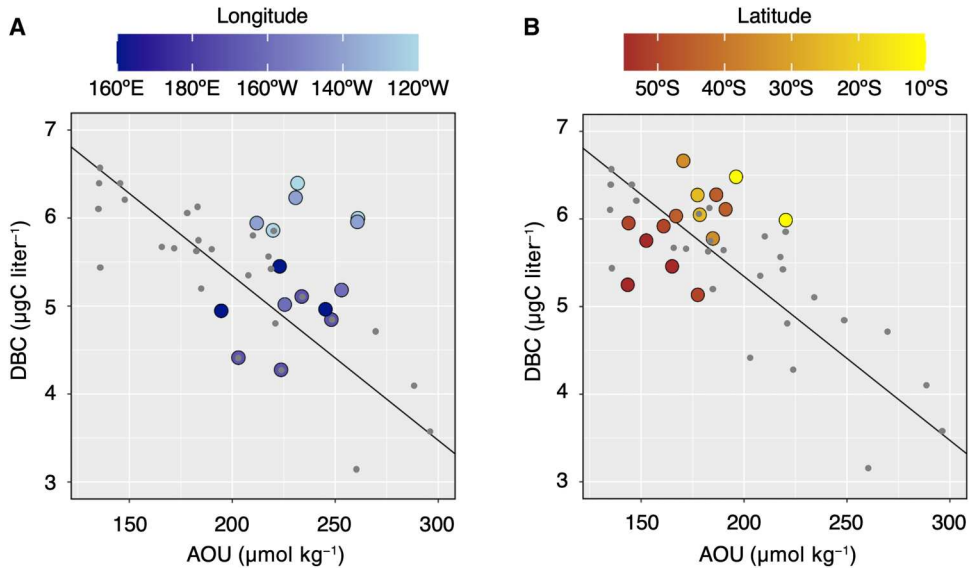

Fig. 3. Relationships between the DBC concentration and AOU in deep waters. (**A**) Relationship in the subtropical North Pacific Ocean (R^2 = 0.081, P = 0.303, n = 15). (**B**) Relationship in the eastern South Pacific Ocean (R^2 = 0.134, P = 0.180, n = 15). The overlaid gray circles and black lines show the data and regression lines ([DBC] = −0.0187 [AOU] + 9.09), respectively, obtained from previous research in the central and western Pacific Ocean (*16*).

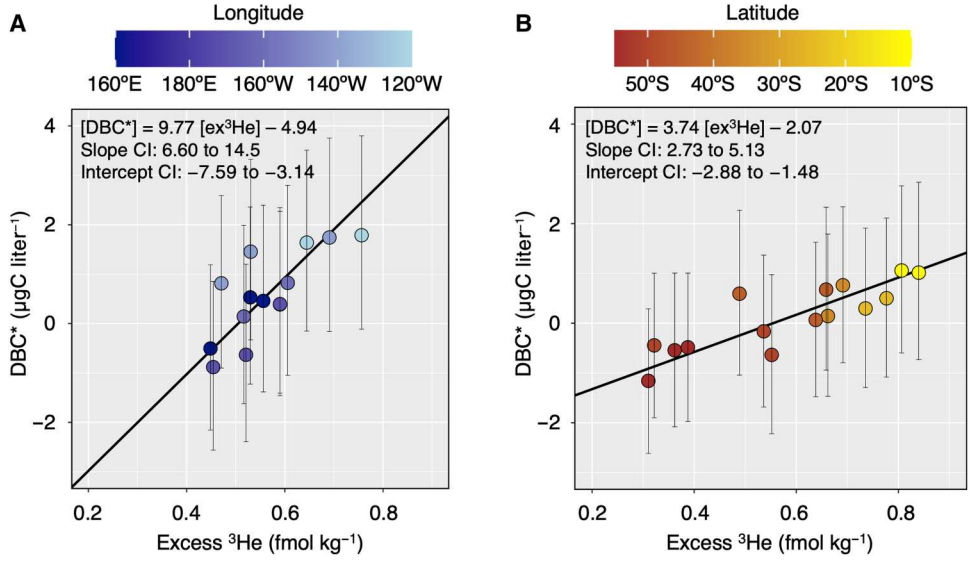

Fig. 4. Relationships between DBC* and excess ^{3}He in deep waters. (**A**) Relationship in the subtropical North Pacific Ocean. (**B**) Relationship in the eastern South Pacific Ocean. The ^{3}He data were derived from Jenkins *et al.* (*30*). The error bars of the plots indicate errors associated with the estimation of DBC* (see Materials and Methods for details). A standard major axis regression was applied to determine the linear relationships between the DBC* and excess ^{3}He, and the relationships are shown as black lines. The 95% confidence intervals (CIs) determined for the slope and the intercept are also described in the figures. The results of the ordinary least squares regression were as follows: [DBC*] = 7.51 [ex^{3}He] − 3.66 (R^2 = 0.590, P = 0.0013, n = 14) for the subtropical North Pacific Ocean (A) and [DBC*] = 3.16 [ex^{3}He] − 1.73 (R^2 = 0.713, P < 0.001, n = 15) for the eastern South Pacific Ocean (B).

(B5CA + B6CA)/total BPCAs (Fig. 5), suggesting that the hydrothermal vents supply highly condensed DBC.

Negative values were observed for DBC*, mainly in the southern part of the eastern South Pacific Ocean; however, the errors associated with the estimation of DBC* concentration were relatively large (Fig. 4). The δ^3He value in the deep water at the southernmost site in the central South Pacific Ocean was higher than that at the southernmost site in the eastern South Pacific Ocean (Fig. 1). Therefore, the negative DBC* observed in the eastern South Pacific Ocean suggests that the DBC concentrations in the linear relationship observed in the central and western Pacific Ocean likely included the DBC derived from hydrothermal vents, and thus, the DBC* was likely underestimated due to an overestimation of the intercept of the linear relationship.

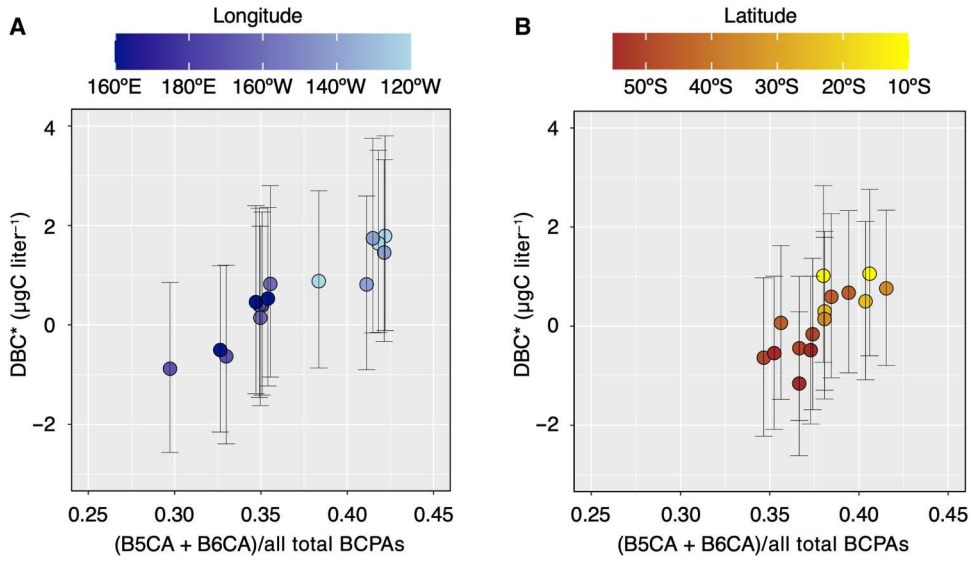

Fig. 5. Relationships between DBC* and the degree of DBC condensation in deep waters. (**A**) Relationship in the subtropical North Pacific Ocean. (**B**) Relationship in the eastern South Pacific Ocean. (B5CA + B6CA)/total BPCAs represents the degree of DBC condensation. A high ratio indicates highly condensed DBC.

Formation pathways for hydrothermal DBC

Dissolved oxygen (DO) in seawater is removed during hydrothermal circulation; however, this signal becomes less detectable because of the dilution of hot hydrothermal fluids with oxygen-rich deep water (Fig. 2). Therefore, mixing of deep seawater with hot hydrothermal fluids, which contain DBC at much higher concentrations, perhaps contributes to DBC*. The formation of DBC may involve the reduction of CO or CO_2 in hydrothermal fluids, as suggested for the formation mechanism of graphite (*28*, *40*). DBC is also likely formed via pyrolysis of DOC and particulate organic carbon in seawater (*10*, *41*, *42*) and/or in deeper deposits (*28*, *41*). Because the apparent radiocarbon age of DBC in the deep ocean is very old (23,000 ± 3000 years) (*27*), the probable formation mechanism for DBC with hydrothermal circulation is the reduction of inorganic carbon or the pyrolysis of organic carbon in deeper deposits.

Previous observations of hydrothermal vent fluids have indicated that aromatic compounds in solid-phase extracted (SPE)–DOC, including DBC, are consumed with hydrothermal circulation (*7*, *10*, *24*), although the degree of condensation increases with the thermal alteration of SPE-DOC (*10*, *24*). However, the basin-scale distributions of DBC and ^{3}He suggest that the highly condensed DBC that is derived from hydrothermal vents, which should have higher concentrations than the deep waters, is transported over long distances (Figs. 2, 4, and 5). The condensed aromatics or aromatic petroleum-like products formed in the hot hydrothermal fluids are suggested to become insoluble (*42*) or be adsorbed/condensed onto inorganic substrates (*41*) during cooling by mixing with seawater, and such particulate BC is outside of the analytical window of SPE-DOC and DBC (*42*). In addition, colloidal aromatics have been shown to dissipate into the water column mainly by dispersion, dissolution, and biodegradation (*41*). Hydrothermal graphite has been suggested to disperse thousands of kilometers from vent sites (*28*). Furthermore, pyrite nanoparticles composed of iron and sulfur that are <200 nm in size (*43*) and nanoparticulate and particulate iron oxyhydroxides (*44*) have been reported to be transported long distances from hydrothermal vents. Thus, the long-distance transport of hydrothermal DBC observed in this study suggests that DBC is likely formed in hot hydrothermal fluids, transformed into colloidal/particle fractions [i.e., insoluble colloidal condensed aromatics and/or condensed aromatics sorbed onto hydrothermal iron (nano)particles] during mixing with seawater and then dissolves or redissociates through oxidation from the colloidal/particulate fractions in the hydrothermal plumes.

Implications of hydrothermal DBC for the marine DOC cycle

The linear regressions between DBC* and excess ^{3}He indicate that hydrothermal DBC is likely transported in the core of the jet-like mid-depth hydrothermal plume and is distributed outside the plume in the eastern Pacific Ocean due to long-distance transport. Hydrothermal DBC can explain the extremely old apparent ^{14}C age of DBC in the deep ocean (23,000 ± 3000 years) (*27*) and is probably a missing DBC source in ocean, which is suggested by the imbalance in the DBC budget in the ocean (*16*, *45*). Furthermore, hydrothermal DBC might be a factor contributing to the linkage between the Δ^{14}C signature of DOC and the excess ^{3}He observed in the eastern Pacific Ocean (*12*, *13*). Because DBC is considered to be biologically recalcitrant (*16*, *17*), it is an important component of hydrothermal RDOC, which can be transported long distances in the deep ocean. Riverine DOC, including DBC, is a well-known source of allochthonous RDOC; however, riverine RDOC and DBC are easily photodegraded by sunlight (*33*, *46*). Therefore, the DBC of deep-sea hydrothermal origin is likely an important source of ^{14}C-depleted allochthonous DOC in the deep oceans that maintains the RDOC pool in the ocean.

Here, we tentatively estimated low and high hydrothermal DBC fluxes from mid-ocean ridges. The slopes with 95% confidence intervals ranging from 2.73×10^9 to 14.5×10^9 gC DBC per mole excess ^{3}He (Fig. 4) were assumed to be the representative range of DBC input from steady-state mid-ocean ridge hydrothermal systems, and the global integrated hydrothermal ^{3}He flux of 585 to 672 mol year^{-1} (*47*) yielded a range of hydrothermal DBC flux

of 1.6×10^{12} to 9.7×10^{12} gC year^{-1}. It should be noted that the lower limit of our tentative estimate is similar to the hydrothermal DBC flux (1.2×10^{12} gC year^{-1}) that was recently used in a box model to evaluate the contribution of hydrothermal DBC to the concentration and apparent ^{14}C age of DBC in the deep ocean (*45*). The model reconstructed the age of DBC well but overestimated the concentration of DBC, suggesting that hydrothermal DBC is a possible source that might explain the ^{14}C age of DBC in the deep ocean, but in addition to DBC removal through sorption to sinking particles (*16*), other DBC sinks might be present in the deep ocean.

The global hydrothermal DBC flux that was tentatively estimated in this study corresponded to 8.9 to 53.9% and 0.6 to 3.9% of the riverine DBC and DOC fluxes to the ocean, respectively (*48*, *49*). However, it should be noted that this estimate likely includes a large bias because the relationships between DBC* and excess ^{3}He are likely nonlinear between the hydrothermal plume and locations outside the plume. Observations of DBC and particulate BC distributions in the EPR hydrothermal plume are necessary to clarify the mechanism of hydrothermal DBC formation and to constrain the DBC flux from hydrothermal vents.

MATERIALS AND METHODS

Sampling and solid phase extraction

Observations along a transect in the subtropical North Pacific Ocean were carried out in August–September 2017 by R/V *Hakuho Maru* (KH-17-4). One site observed by R/V *Hakuho Maru* (KH-14-3) in July 2014 was added to the transect. Observations along a transect in the eastern South Pacific Ocean were conducted in November–December 2019 by R/V *Hakuho Maru* (KH-19-6). Salinity and temperature were measured using a conductivity-temperature-depth (CTD) sensor. DO concentrations were determined using an oxygen sensor that was calibrated using DO concentrations determined by the Winkler titration method. Oxygen solubility was calculated according to Weiss (*50*), and AOU was calculated as the difference between the saturated and measured DO concentrations. The temperature, salinity, DO, and DBC results at site St11 from the KH-17-4 survey and site ST05 from the KH-14-3 survey have been reported in another publication (*16*).

Seawater samples were collected at depths ranging from the surface layer to the deep layer with 12-L acid-cleaned, Teflon-coated Niskin-X bottles that were mounted on the CTD sensor with a carousel multisampling system. The seawater was filtered using a precombusted (450°C, 3 to 5 hours) glass fiber filter of a 0.7-μm nominal pore size (GF/F, Whatman). Immediately after sampling, the pH of the filtrate was adjusted to 2 with a concentrated HCl. The dissolved organic matter in the acidified filtrate was extracted by a solid-phase extraction (SPE) method using a cartridge (Bond Elut PPL, Agilent Technologies) according to a method by Dittmar *et al.* (*51*). The SPE cartridge was stored at −20°C in the dark (*20*).

DBC analysis

The organic matter adsorbed in the SPE cartridge was eluted using two cartridge volumes of MeOH according to the method described in Dittmar *et al.* (*51*). The extraction efficiency was reported to be approximately 40% for DOC in the open ocean (*51*). The eluate was poured into a glass vial with a Teflon-lined cap and then stored in the dark in a freezer (−20°C).

DBC analysis was performed with the BPCA method using the procedures detailed by Dittmar (*15*) with some modifications (*21*). Briefly, the MeOH eluate was transferred into a glass ampoule and completely dried, and then concentrated HNO_3 was added. The ampoule was flame-sealed and kept in an oven at 170°C for 6 hours according to the method by Nakane *et al.* (*20*). After 9 hours at an oxidation temperature of 170°C, the losses of BPCAs were reported to be insignificant (*15*). Then, the HNO_3 was evaporated to dryness. The samples in the ampoules were redissolved in mobile phase A (as described below) for BPCA analysis with a high-performance liquid chromatography (HPLC) equipped with a photodiode array detector (1260 Infinity, Agilent).

The DBC analytical method carried out by HPLC was based on Nakane *et al.* (*20*). Two mobile phases, namely, mobile phase A (4 mM tetrabutylammonium bromide, 50 mM sodium acetate, and 10% MeOH) and mobile phase B (MeOH), were used for separation of the BPCAs with a C_{18} column (3.5 μm, 2.1 × 150 mm, Sunfire, Waters) and a guard column (3.5 μm, 2.1 × 10 mm, Sunfire, Waters). Each BPCA was identified by retention time and its absorbance spectrum and quantified with the absorbance at 235 nm. The column oven and autosampler were set to 16° and 4°C, respectively.

The DBC concentration was calculated from the BPCA concentrations using Eq. 1 proposed by Dittmar (*15*)

$$[\mathrm{DBC}] = 12.01 \times 33.4\,([\mathrm{B6CA}] + [\mathrm{B5CA}] + 0.5[\mathrm{B4CA}] + 0.5[\mathrm{B3CA}]) \quad (1)$$

The units of [DBC] and [BPCAs] were micrograms of carbon per liter and micromoles per liter, respectively. The analytical error of the method using triplicate seawater samples was <4% (*20*). The ratio of B5CA and B6CA to the total BPCAs [(B5CA + B6CA)/total BPCAs)] was calculated as an index for the degree of DBC condensation.

Helium data

All of the helium concentrations and δ^3He values used in this study were obtained from a comprehensive dataset (*30*). The helium data for the sampling sites and depths closest to those in the present study were collected manually and are listed in data file S1.

Excess ^{3}He (femtomoles per kilogram) was calculated as an approximate measure of the nonatmospheric ^{3}He over saturation according to Resing *et al.* (*31*).

$$[\text{Excess } ^3\mathrm{He}] = (\delta^3\mathrm{He} - \delta^{*3}\mathrm{He})/100 \times [\mathrm{He}] \times 1.384 \times 10^{-6} \quad (2)$$

where δ^{*3}He is the helium isotope ratio anomaly in solubility equilibrium with the atmosphere that is a weak function of temperature (*52*). The potential temperature calculated from the δ^3He dataset was used to estimate δ^{*3}He. [He] is the helium concentration (nanomoles per kilogram), and 1.384×10^{-6} is the ^{3}He/^{4}He ratio of the air.

The ^{3}He samples that were obtained from locations closest to our observation sites were collected over 1974–1991 in the North Pacific Ocean and over 1993–1994 in the South Pacific Ocean. Observations showed that the ^{3}He values around the EPR in the South Pacific Ocean remained unchanged over three decades (1987–2013), except in some sites near the EPR axis (*37*). Because our sampling sites were relatively far from the EPR axis, the ^{3}He values at our study sites in 2017 and 2019 might be largely consistent with

those reported during previous time periods. Furthermore, using the ^{3}He dataset (*30*), we evaluated the space/time variations in excess ^{3}He at sites close to the sampling sites Stn1 (relatively close to the EPR axis) and Stn6 (far from the EPR axis) in the Southern Pacific Ocean (fig. S2) in this study. The differences in excess ^{3}He between the sites and observational periods were relatively small compared with the large error in DBC* (Fig. 4). These results suggest that space/time differences between ^{3}He and DBC observations disrupted the relationship between DBC* and excess ^{3}He, but the effect is probably negligible.

Calculations of the hydrothermal DBC concentration (DBC*)

A negative linear regression has been found between the DBC concentration and AOU in deep waters ([DBC] = −0.0187 [AOU] + 9.09) in the central and western Pacific Ocean (*16*). Here, samples from the deep waters did not follow the linear regression and exhibited deviations from the linear regression (Fig. 3). The deviation from linear regression was likely due to the contribution of DBC from hydrothermal systems, and the value is defined as DBC*. DBC* was estimated from the DBC concentration, AOU, and the linear regression determined in the central and western Pacific Ocean (*16*) as follows

$$[\mathrm{DBC}^*] = [\mathrm{DBC}] - (-0.0187 \times [\mathrm{AOU}] + 9.09)$$

Errors associated with the estimation of DBC* were estimated using the 95% confidence intervals for the slope (−0.0235 to −0.0149) and intercept (8.33 to 10.0) of the linear regression (*16*). Thus, all DBC* values have relatively large but proportional errors derived from the 95% confidence intervals, indicating that the interpretation of the linear regression between DBC* and excess ^{3}He is valid. However, it should be noted that the slope and intercept of the regression between DBC* and excess ^{3}He may contain large uncertainties.

Statistical analysis and mapping

Standard major axis regression was carried out using the lmodel2 package (version 1.7-3) (*53*) in R (version 4.0.4). The *P* value of the two-tailed test was reported. Ocean Data View (version 5.1.5) (*54*) was used to produce the map and basin-scale distributions of each parameter in Figs. 1 and 2 and fig. S2.

Supplementary Materials

This PDF file includes:
Figs. S1 and S2
Legends for data S1 and S2

Other Supplementary Material for this manuscript includes the following:
Data S1 and S2

REFERENCES AND NOTES

1. D. A. Hansell, C. A. Carlson, D. J. Repeta, R. Schlitzer, Dissolved organic matter in the ocean: A controversy stimulates new insights. *Oceanography* **22**, 202–211 (2009).
2. J. E. Bauer, P. M. Williams, E. R. M. Druffel, ^{14}C activity of dissolved organic carbon fractions in the north-central Pacific and Sargasso Sea. *Nature* **357**, 667–670 (1992).
3. E. R. M. Druffel, P. M. Williams, J. E. Bauer, J. R. Ertel, Cycling of dissolved and particulate organic matter in the open ocean. *J. Geophys. Res.* **97**, 15639–15659 (1992).
4. S. Opsahl, R. Benner, Distribution and cycling of terrigenous dissolved organic matter in the ocean. *Nature* **386**, 480–482 (1997).
5. T. Dittmar, S. T. Lennartz, H. Buck-Wiese, D. A. Hansell, C. Santinelli, C. Vanni, B. Blasius, J.-H. Hehemann, Enigmatic persistence of dissolved organic matter in the ocean. *Nat. Rev. Earth Environ.* **2**, 570–583 (2021).
6. S. Q. Lang, D. A. Butterfield, M. D. Lilley, H. P. Johnson, J. I. Hedges, Dissolved organic carbon in ridge-axis and ridge-flank hydrothermal systems. *Geochim. Cosmochim. Acta* **70**, 3830–3842 (2006).
7. J. A. Hawkes, P. E. Rossel, A. Stubbins, D. Butterfield, D. P. Connelly, E. P. Achterberg, A. Koschinsky, V. Chavagnac, C. T. Hansen, W. Bach, T. Dittmar, Efficient removal of recalcitrant deep-ocean dissolved organic matter during hydrothermal circulation. *Nat. Geosci.* **8**, 856–860 (2015).
8. K. Longnecker, S. M. Sievert, S. P. Sylva, J. S. Seewald, E. B. Kujawinski, Dissolved organic carbon compounds in deep-sea hydrothermal vent fluids from the East Pacific Rise at 9° 50′N. *Org. Geochem.* **125**, 41–49 (2018).
9. H.-T. Lin, D. J. Repeta, L. Xu, M. S. Rappé, Dissolved organic carbon in basalt-hosted deep subseafloor fluids of the Juan de Fuca Ridge flank. *Earth Planet. Sci. Lett.* **513**, 156–165 (2019).
10. P. E. Rossel, A. Stubbins, T. Rebling, A. Koschinsky, J. A. Hawkes, T. Dittmar, Thermally altered marine dissolved organic matter in hydrothermal fluids. *Org. Geochem.* **110**, 73–86 (2017).
11. M. D. McCarthy, S. R. Beaupré, B. D. Walker, I. Voparil, T. P. Guilderson, E. R. M. Druffel, Chemosynthetic origin of 14C-depleted dissolved organic matter in a ridge-flank hydrothermal system. *Nat. Geosci.* **4**, 32–36 (2011).
12. G. W. Luther III, Hydrothermal vents are a source of old refractory organic carbon to the deep ocean. *Geophys. Res. Lett.* **48**, e2021GL094869 (2021).
13. E. R. M. Druffel, S. Griffin, C. B. Lewis, M. Rudresh, N. G. Garcia, R. M. Key, A. P. McNichol, N. E. Hauksson, B. D. Walker, Dissolved organic radiocarbon in the Eastern Pacific and Southern Oceans. *Geophys. Res. Lett.* **48**, e2021GL092904 (2021).
14. T. Dittmar, B. P. Koch, Thermogenic organic matter dissolved in the abyssal ocean. *Mar. Chem.* **102**, 208–217 (2006).
15. T. Dittmar, The molecular level determination of black carbon in marine dissolved organic matter. *Org. Geochem.* **39**, 396–407 (2008).
16. Y. Yamashita, M. Nakane, Y. Mori, J. Nishioka, H. Ogawa, Fate of dissolved black carbon in the deep Pacific Ocean. *Nat. Commun.* **13**, 307 (2022).
17. K. W. Bostick, A. R. Zimmerman, A. I. Goranov, S. Mitra, P. G. Hatcher, A. S. Wozniak, Biolability of fresh and photodegraded pyrogenic dissolved organic matter from laboratory-prepared chars. *J. Geophys. Res.* **126**, e2020JG005981 (2021).
18. T. Dittmar, J. Paeng, A heat-induced molecular signature in marine dissolved organic matter. *Nat. Geosci.* **2**, 175–179 (2009).
19. S. Wagner, J. Brandes, R. G. M. Spencer, K. Ma, S. Z. Rosengard, J. M. S. Moura, A. Stubbins, Isotopic composition of oceanic dissolved black carbon reveals non-riverine source. *Nat. Commun.* **10**, 5064 (2019).
20. M. Nakane, T. Ajioka, Y. Yamashita, Distribution and sources of dissolved black carbon in surface waters of the Chukchi Sea, Bering Sea, and the North Pacific Ocean. *Front. Earth Sci.* **5**, 34 (2017).
21. Y. Mori, J. Nishioka, S. Fujio, Y. Yamashita, Transport of dissolved black carbon from marginal sea sediments to the western North Pacific. *Prog. Oceanogr.* **193**, 102552 (2021).
22. Z. Fang, W. Yang, M. Chen, A. Stubbins, H. Ma, R. Jia, Q. Li, Q. Chen, Transport of dissolved black carbon from the Prydz Bay Shelf, Antarctica to the deep Southern Ocean. *Limnol. Oceanogr.* **63**, 2179–2190 (2018).
23. Z. Fang, W. Yang, A. Stubbins, M. Chen, J. Li, R. Jia, Q. Li, J. Zhu, B. Wang, Spatial characteristics and removal of dissolved black carbon in the western Arctic Ocean and Bering Sea. *Geochim. Cosmochim. Acta* **304**, 178–190 (2021).
24. J. Niggemann, J. A. Hawkes, P. E. Rossel, A. Stubbins, T. Dittmar, Hydrothermal systems are a sink for dissolved black carbon in the deep ocean. *Ocean Science Meeting Abstracts*. CT44A-0211 (2016).
25. S. Wagner, R. Jaffé, A. Stubbins, Dissolved black carbon in aquatic ecosystems. *Limnol. Oceanogr. Lett.* **3**, 168–185 (2018).
26. C. Santín, S. H. Doerr, E. S. Kane, C. A. Masiello, M. Ohlson, J. M. de la Rosa, C. M. Preston, T. Dittmar, Towards a global assessment of pyrogenic carbon from vegetation fires. *Glob. Chang. Biol.* **22**, 76–91 (2016).
27. A. I. Coppola, E. R. M. Druffel, Cycling of black carbon in the ocean. *Geophys. Res. Lett.* **43**, 4477–4482 (2016).
28. E. R. Estes, D. Berti, N. R. Coffey, M. F. Hochella Jr., A. S. Wozniak, G. W. Luther III, Abiotic synthesis of graphite in hydrothermal vents. *Nat. Commun.* **10**, 5179 (2019).
29. H. Craig, W. B. Clarke, M. A. Beg, Excess ^{3}He in deep water on the East Pacific Rise. *Earth Planet. Sci. Lett.* **26**, 125–132 (1975).
30. W. J. Jenkins, S. C. Doney, M. Fendrock, R. Fine, T. Gamo, P. Jean-Baptiste, R. Key, B. Klein, J. E. Lupton, R. Newton, M. Rhein, W. Roether, Y. Sano, R. Schlitzer, P. Schlosser, J. Swift, A

comprehensive global oceanic dataset of helium isotope and tritium measurements. *Earth Syst. Sci. Data* **11**, 441–454 (2019).
31. J. A. Resing, P. N. Sedwick, C. R. German, W. J. Jenkins, J. W. Moffett, B. M. Sohst, A. Tagliabue, Basin-scale transport of hydrothermal dissolved metals across the South Pacific Ocean. *Nature* **523**, 200–203 (2015).
32. A. Stubbins, J. Niggemann, T. Dittmar, Photo-lability of deep ocean dissolved black carbon. *Biogeosciences* **9**, 1661–1670 (2012).
33. S. Wagner, R. Jaffé, Effect of photodegradation on molecular size distribution and quality of dissolved black carbon. *Org. Geochem.* **86**, 1–4 (2015).
34. Y. Ding, Y. Yamashita, J. Jones, R. Jaffe, Dissolved black carbon in boreal forest and glacial rivers of central Alaska: Assessment of biomass burning versus anthropogenic sources. *Biogeochem.* **123**, 15–25 (2015).
35. T. Takemura, T. Nozawa, S. Emori, T. Y. Nakajima, T. Nakajima, Simulation of climate response to aerosol direct and indirect effects with aerosol transport-radiation model. *J. Geophys. Res.* **110**, D02202 (2005).
36. J. E. Lupton, H. Craig, A major helium-3 source at 15°S on the East Pacific Rise. *Science* **214**, 13–18 (1981).
37. J. E. Lupton, W. J. Jenkins, Evolution of the south Pacific helium plume over the past three decades. *Geochem. Geophys. Geosyst.* **18**, 1810–1823 (2017).
38. W. J. Jenkins, D. E. Lott III, C. R. German, K. L. Cahill, J. Goudreau, B. Longworth, The deep distributions of helium isotopes, radiocarbon, and noble gases along the U.S. GEOTRACES East Pacific Zonal Transect (GP16). *Mar. Chem.* **201**, 167–182 (2018).
39. N. Takahata, M. Agarwal, M. Nishizawa, K. Shirai, Y. Inoue, Y. Sano, Helium-3 plume over the East Pacific Rise at 25°S. *Geophys. Res. Lett.* **32**, L11608 (2005).
40. J. Jedwab, J. Boulègue, Graphite crystals in hydrothermal vents. *Nature* **310**, 41–43 (1984).
41. B. R. T. Simoneit, Aqueous high-temperature and high-pressure organic geochemistry of hydrothermal vent systems. *Geochim. Cosmochim. Acta* **57**, 3231–3243 (1993).
42. J. A. Hawkes, C. T. Hansen, T. Goldhammer, W. Bach, T. Dittmar, Molecular alteration of marine dissolved organic matter under experimental hydrothermal conditions. *Geochim. Cosmochim. Acta* **175**, 68–85 (2016).
43. M. Yücel, A. Gartman, C. S. Chan, G. W. Luther III, Hydrothermal vents as a kinetically stable source of iron-sulphide-bearing nanoparticles to the ocean. *Nat. Geosci.* **4**, 367–371 (2011).
44. J. N. Fitzsimmons, S. G. John, C. M. Marsay, C. L. Hoffman, S. L. Nicholas, B. M. Toner, C. R. German, R. M. Sherrell, Iron persistence in a distal hydrothermal plume supported by dissolved-particulate exchange. *Nat. Geosci.* **10**, 195–201 (2017).
45. A. I. Coppola, S. Wagner, S. T. Lennartz, M. Seidel, N. D. Ward, T. Dittmar, C. Santín, M. W. Jones, The black carbon cycle and its role in the Earth system. *Nat. Rev. Earth Environ.* **3**, 516–532 (2022).
46. M. A. Moran, W. A. Sheldon Jr., R. G. Zepp, Carbon loss and optical property changes during long-term photochemical and biological degradation of estuarine dissolved organic matter. *Limnol. Oceanogr.* **45**, 1254–1264 (2000).
47. T. DeVries, M. Holzer, Radiocarbon and helium isotope constraints on deep ocean ventilation and mantle-^{3}He sources. *J. Geophys. Res.* **124**, 3036–3057 (2019).
48. J. I. Hedges, R. G. Keil, R. Benner, What happens to terrestrial organic matter in the ocean? *Org. Geochem.* **27**, 195–212 (1997).
49. M. W. Jones, A. I. Coppola, C. Santín, T. Dittmar, R. Jaffé, S. H. Doerr, T. A. Quine, Fires prime terrestrial organic carbon for riverine export to the global oceans. *Nat. Commun.* **11**, 2791 (2020).
50. R. F. Weiss, The solubility of nitrogen, oxygen and argon in water and seawater. *Deep-Sea Res. Oceanogr. Abstr.* **17**, 721–735 (1970).
51. T. Dittmar, B. Koch, N. Hertkorn, G. Kattner, A simple and efficient method for the solid-phase extraction of dissolved organic matter (SPE-DOM) from seawater. *Limnol. Oceanogr.: Methods* **6**, 230–235 (2008).
52. B. B. Benson, D. J. Krause, Isotopic fractionation of helium during solution: A probe for the liquid state. *J. Solution Chem.* **9**, 895–909 (1980).
53. P. Legendre, lmodel2: Model II regression. R package version 1.7-3, 2018; https://cran.r-project.org/web/packages/lmodel2/index.html.
54. R. Schlitzer, Ocean Data View, 2020; http://odv.awi.de.

Acknowledgments: We would like to thank the captain, crew, principal investigators, and scientists onboard the R/V *Hakuho Maru* for their help with the observations, as well as S. Goto, F. Hashihama, and J. Nishioka for help with water sampling. **Funding:** This work was supported by Japan Society for the Promotion of Science grants KAKENHI JP16H02930, KAKENHI JP19H04249, and KAKENHI JP22H03714 to Y.Y., and Japan Society for the Promotion of Science grants KAKENHI JP19H05667 and KAKENHI JP19H04260 to H.O. **Author contributions:** Conceptualization: Y.Y. and Y.M. Investigation: Y.M. Formal analysis: Y.Y. Resources: Y.Y. and H.O. Visualization: Y.Y. Supervision: Y.Y. Writing—original draft: Y.Y. Writing—review and editing: Y.Y. and H.O. **Competing interests:** The authors declare that they have no competing interests. **Data and materials availability:** All data needed to evaluate the conclusions in the paper are present in the paper and/or the Supplementary Materials.

Submitted 12 August 2022
Accepted 6 January 2023
Published 10 February 2023
10.1126/sciadv.ade3807